metals

MDPI

Article

The Effect of Stearic Acid on Microstructure and Properties of $(Ti_2AlC + Al_2O_3)_p$/TiAl Composites

Jiawei Zhu [1], Meini Yuan [1,*], Xin Pei [2], Xiaosheng Zhou [3] and Maohua Li [4]

[1] The School of Aerospace Engineering, North University of China, Taiyuan 030051, China; zjw2408813362@163.com
[2] The School of Mechanical and Electrical Engineering, North University of China, Taiyuan 030051, China; px2565586030@163.com
[3] The School of Mechanical Engineering, North University of China, Taiyuan 030051, China; tjuzhouxs@163.com
[4] The School of Materials Science and Engineering, Hunan University of Science and Technology, Xiangtan 411201, China; mhli@hnust.edu.cn
* Correspondence: mnyuan@nuc.edu.cn

Abstract: A new type of multiphase nanoparticle-reinforced TiAl matrix composites ($(Ti_2AlC + Al_2O_3)_p$/TiAl composites) was successfully prepared by vacuum hot-pressing sintering using Ti powder and Al powder, which were ball-milled with different contents of stearic acid ($CH_3(CH_2)_{16}COOH$). The component, microstructure, reaction mechanism, and mechanical properties were studied. The results indicated that the composites prepared by adding stearic acid as a process control agent during the ball-milling process not only contained γ-TiAl and α_2-Ti_3Al phases but also Ti_2AlC and Al_2O_3 phases. The results of SEM and TEM showed that the composites were composed of equiaxed TiAl and Ti_3Al grains, and the Ti_2AlC and Al_2O_3 particles were mainly distributed along the TiAl grain boundary in chain form, which can effectively reduce the TiAl grain size. Through the room-temperature compression test, the maximum compression stress was significantly improved in those composites that added the stearic acid, due to the reinforcement particles. The maximum compression stress was 1590 MPa with a 24.3% fracture strain. In addition, the generated crack deflection and Ti_2AlC and Al_2O_3 particles could also enhance the toughness of the TiAl alloy. $(Ti_2AlC + Al_2O_3)_p$/TiAl composites generated by adding stearic acid played a key role in improving the mechanical properties of the TiAl matrix.

Keywords: TiAl intermetallic; titanium carbide; process control agent; microstructure; mechanical properties

Citation: Zhu, J.; Yuan, M.; Pei, X.; Zhou, X.; Li, M. The Effect of Stearic Acid on Microstructure and Properties of $(Ti_2AlC + Al_2O_3)_p$/TiAl Composites. *Metals* **2024**, *14*, 392. https://doi.org/10.3390/met14040392

Academic Editor: Daniela Pilone

Received: 24 February 2024
Revised: 21 March 2024
Accepted: 25 March 2024
Published: 27 March 2024

1. Introduction

The theoretical density of TiAl intermetallic compounds is only 3.9 g/cm^3, which is less than half of that of nickel-based high-temperature alloys. It not only meets the requirements of aviation light-weighting but also has excellent mechanical properties. The TiAl alloy has better specific tensile strength than nickel-based alloys in the temperature range of 700–850 °C [1–3]. It is the only lightweight metal material that can be used for a long time in oxidation environments above 600 °C, providing a possible new material to replace traditional high-temperature alloys. However, the room-temperature brittleness and poor toughness of the TiAl alloy severely limit its wider engineering applications [4,5]. To promote its widespread application in practical production, research on the strengthening and toughening of TiAl alloys has become one of the current research hotspots.

In the study of strengthening and toughening TiAl alloys, traditional strengthening methods such as alloying or heat treatment are used to optimize preparation processes. However, these methods all have a trade-off between strength and toughness [6–8]. Research has shown that by introducing high-strength nanocrystalline [9,10] or ultrafine grain structures [11,12] into TiAl alloys, the trade-off between strength and toughness can be

effectively avoided. However, these methods have problems, such as high production process costs, low efficiency, and immature technology [13]. Compared with the above methods, this study adopts the composite material method of introducing nanomicron particles into the TiAl matrix to improve the comprehensive performance of the TiAl alloy. This not only ensures a certain strength but also improves its toughness, which is considered one of the simplest and most effective methods.

In the composite material method, the powder metallurgy method of mechanical ball milling combined with subsequent sintering is often used to prepare TiAl matrix composites due to their economical, controllable material composition and microstructure [14,15]. Stearic acid ($C_{18}H_{36}O_2$) can inhibit the excessive cold-welding behavior of powder during mechanical ball milling and avoid powder bonding [16]. In addition, stearic acid serves as a process control agent to provide carbon and oxygen sources to generate Ti_2AlC and Al_2O_3 particles. This has a certain impact on the microstructure and properties of TiAl matrix composites that researchers often neglect.

The ternary nanolayered compound $M_{n+1}AX_n$ phase (also known as MAX phase) and ceramic particles are commonly used as reinforcing phases in TiAl matrix composites. MAX compound Ti_2AlC has a similar density (Ti_2AlC—4.11 g/cm^3, TiAl—3.8 g/cm^3) and thermal expansion coefficient (Ti_2AlC—8.8 × 10^{-6} K^{-1}, TiAl—12.2 × 10^{-6} K^{-1}) to TiAl matrix [17], which combines ceramic and metal properties [18] and has good interface bonding and low internal stress at the interface. When Ti_2AlC particles are used to enhance TiAl matrix composites, they can effectively reduce the thermal residual stress between the reinforcing particles and the matrix, making it one of the ideal reinforcements for TiAl matrix composites. Chen et al. [19] successfully prepared Ti_2AlC-reinforced TiAl matrix composites and studied their fracture behavior. They found that the layered structure of Ti_2AlC comprehensively improved the mechanical properties of the TiAl alloy. The maximum strength of the Ti_2AlC/TiAl composites' compression testing increased by 38%, and their maximum fracture strain increased by 121.37%. Shu et al. [20] prepared Ti_2AlC/TiAl composites using hot-pressing sintering technology, with a maximum compressive strength of 1435 MPa, which is 334 MPa higher than that of ordinary TiAl alloys. Cheng et al. [21] prepared near-mesh Ti_2AlC-reinforced TiAl matrix composites and found that the bending strength of the TiAl composite first increased and then decreased with the increase in Ti_2AlC content, while the hardness increased. In addition, the reinforced particle distribution of near-mesh Ti_2AlC effectively improved the wear resistance of TiAl compared with TiAl-based alloys.

Ceramic particles such as Al_2O_3 [22], TiC [23], SiO_2 [24], TiB_2 [25], and SiC [26] are often used as reinforcing phases in TiAl matrix composites. These hard reinforcing phases can effectively improve the strength, hardness, and other properties of TiAl matrix composites. Among them, Al_2O_3 has high strength and hardness, relatively low material cost, and a similar thermal expansion coefficient to TiAl matrix composites. Using Al_2O_3 particles to enhance TiAl matrix composites can significantly improve high-temperature strength, oxidation resistance, wear resistance, corrosion resistance, and other aspects [27,28]. Huy et al. [29] prepared Al_2O_3/$TiAl_3$ composites by the in situ method. Through hardness testing, it was found that the microhardness of Al_2O_3/$TiAl_3$ was significantly increased compared to pure $TiAl_3$, from 450 HV to 800 HV. At the same time, the fracture toughness of $TiAl_3$ increased from 2% to 4%. Lu et al. [30] prepared Al_2O_3/TiAl composites by the hot-pressing method and studied the effect of Al_2O_3 content on the compressive performance of Al_2O_3/TiAl composites. Research has shown that when the Al_2O_3 content is 0.5 wt.%, the maximum fracture strength of Al_2O_3/TiAl composites reaches 2668 MPa. In addition, with the increase of Al_2O_3 content, the yield strength and hardness of Al_2O_3/TiAl composites also improve.

In order to enhance the strength and toughness of the TiAl alloy, a new type of multiphase nanoparticle-reinforced TiAl matrix composite ((Ti_2AlC + Al_2O_3)$_p$/TiAl composites) was successfully prepared by adding different contents of stearic acid during ball milling combined with the vacuum hot-pressing sintering method. So far, research on the process

control agents added during mechanical alloying has mainly focused on the influence of ball milling on powder morphology and powder yield, while there has been no in-depth study on the impact on subsequent sintering products. The microstructure evolution and mechanical properties of $(Ti_2AlC + Al_2O_3)_p$/TiAl composites were systematically studied in this study, and the effect of stearic acid as a control agent in the ball-milling process on the final product was deeply explored. It provides a reference for the preparation of other TiAl matrix composites using this process, which has important referential and scientific significance.

2. Experimental Methods

The as-received Ti and Al powders (99.7% purity), with an average particle size of 45 μm (ZhongNuo Advanced Material (Beijing) Technology Co., Ltd., Beijing, China), were used as the raw materials for milling. The total weight of the powder is 10 g. The mixed Ti-50at.%Al powders (weighing powder: 6.395 g of Ti powder, 3.605 g of Al powder, and 0–0.300 g of stearic acid) with 0 wt.%, 1 wt.%, 2 wt.%, and 3 wt.% stearic acid ($CH_3(CH_2)_{16}COOH$) and tungsten carbide milling balls with a diameter of 4 mm were put into the tungsten carbide milling vial for milling via the BM40 planetary ball mill in an argon atmosphere, where the ratio of balls to elemental powders was 10:1. In order to acquire a composite with a refined and uniform chemical microstructure, the rotation speed was 200 rpm/min, and the milling time was 10 h. After a high-energy ball mill, the ball-milled powders were sintered in the ZT-40-21Y vacuum hot-pressing sintering furnace at a temperature of 1150 °C and subjected to a pressure of 30 MPa at a vacuum condition for two hours. The obtained samples (with 2 wt.% stearic acid) are shown in Figure 1, with sample sizes of Φ 20 mm × 10 mm. In addition, one out of every three samples was used for room-temperature compression testing, and the number of compression tests for each sample prepared with different amounts of stearic acid added was one. The weight and density of the sample measured after sintering with different amounts of stearic acid added in ball milling are shown in the Table 1.

Figure 1. Sample structure of $(Ti_2AlC + Al_2O_3)_p$/TiAl composites.

Table 1. Density of sintered samples with different stearic acid additions.

The Amount of Stearic Acid Added	0 wt.%	1 wt.%	2 wt.%	3 wt.%
Sample weight (g)	10.02	9.93	10.03	10.00
Density (g/cm^3)	3.90	3.86	3.91	3.89

The specific steps of the hot-pressing sintering process are as follows: (1) Put the mixed powder after ball milling into the graphite mold, and then place the graphite mold with powder into a vacuum hot-pressing furnace. Use a pressure of 2 t (62 MPa) to pre-press the powder for 10 min; (2) Use a diffusion pump to extract air from the furnace until the pressure inside the furnace drops to 1.6×10^{-2} Pa, then fill the furnace with high-purity argon as a protective gas, and then start sintering; (3) Raise the temperature inside the furnace to 500 °C at a heating rate of 10 °C/min with a pressure of 1.6 t (32 MPa), and maintain the insulation and pressure for 2 h. When the temperature rises to around 660 °C, unload the pressure. Finally, when the temperature rises to 950–1250 °C, slowly lower the upper pressure head at a speed of 0.01 mm/s. When the displacement does not decrease,

stop lowering the pressure head and adjust the sintering pressure to 1.6 t (about 30 MPa) for insulation and pressure retention for 2 h; (4) After the insulation and pressure preservation are completed, cool down to 500 °C and release the pressure for 2 h, then cool down with the furnace.

The phase of the ball-milled powders and the composites was identified by X-ray diffraction (XRD, Rigaku Smartlab, Cambridge, MA, USA) with Cu-Kα radiation (Kα = 1.542 nm). The microstructure morphology of the composites, the ball-milled powders, and the fracture surface was characterized by scanning electron microscopy (SEM) and transmission electron microscopy (TEM, JEOL Ltd., Tokyo, Japan). The distribution of the elements was investigated by the Energy Dispersive Spectrometer (EDS). The thermal analysis of the mixed powder was carried out using synchronous thermalgravimetry (TG) and differential scanning calorimetry (DSC) (TG-DSC, STA 449 F3 Jupiter, Netzsch, Selb, Germany). The temperature range was from room temperature to 1200 °C at a rate of 20 °C/min, and the heating was in the Ar atmosphere. To study the room-temperature compressive properties of the composites, the room-temperature compression test was performed by the electronic universal testing machine (Metex Industrial Systems (China) Co., Ltd., Shenzhen, China) at a strain rate of 1×10^{-3} s^{-1}.

To measure the hardness of $(Ti_2AlC + Al_2O_3)_p/TiAl$ composites, the sintered material was first cut to obtain a test sample with a size of 5 mm × 5 mm × 6 mm (length × width × height). Second, the tested surface of the specimen was mechanically polished to a mirror surface for the convenience of observing the diagonal length value of the indentation. Finally, the HVS-1000 Micro-Vickers hardness tester (Lgtester, Jinan, China) was used to perform hardness testing on the polished sample. The test load was 500 g, and the loading time was maintained for 10 s. A total of 5–10 data points were equidistant from each sample for hardness testing, and the diagonal length of the indentation at each point was recorded. The average value was taken, and the hardness value of the sample was obtained according to the microhardness calculation formula in Equation (1):

$$HV = 1.8544 \times \frac{1000 \times 9.8}{l_1 \times l_2} \quad (1)$$

This study used the CMT5105 microcomputer-controlled electronic universal testing machine (as shown in Figure 2) to conduct compression tests on the $(Ti_2AlC + Al_2O_3)_p/TiAl$ composites prepared. Three cylindrical specimens with dimensions of Φ 4 mm × 6 mm were cut from the sintered material, and the upper and lower surfaces were simply polished. Then, the compressed specimens were subjected to room-temperature compression testing at a strain rate of 0.25/min.

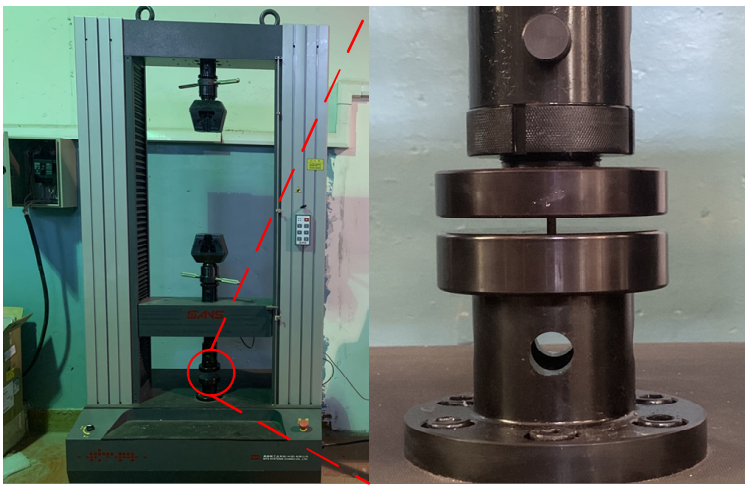

Figure 2. Electronic universal testing machine (Metex Industrial Systems (China) Co., Ltd.).

3. Results and Discussion

3.1. Morphology of TiAl Ball-Milled Powders

Figure 3 shows the morphology of TiAl ball-milled powders without adding 2 wt.% stearic acid. As shown in Figure 3a, the surface of the grinding balls was coated with a layer of ball-milled products with metallic luster. Additionally, some fine, spherical, and flaky ball-milled products can be observed. This phenomenon was attributed to the severe cold welding of ductile aluminum powder. During the ball-milling process, the Ti and Al powder mixture suffered from the impact of grinding balls at high speed. Mass fresh surfaces of TiAl powders (Stanford Advanced Materials (SAM), Lake Forest, CA, USA) were produced, and their surface energy increased, which was conducive to joining together powders, as well as joining powders and the inner wall of the milling vial and the surface of the grinding ball. This resulted in an increase in the collision probability between the grinding balls, and the temperature of the milling vial rose rapidly. As the temperature approached the melting point of Al, Al powder melted and adhered to the surface of the milling vial and grinding balls. When the thickness of the TiAl powders adhered to the surface of the grinding balls increased, part of the adherent TiAl ball-milled powders on the surface of the grinding balls fell off under the impact of the grinding balls and formed a flaky morphology. Some TiAl ball-milled powders presented spherical particle morphology due to the effect of the surface tension of molten Al liquid.

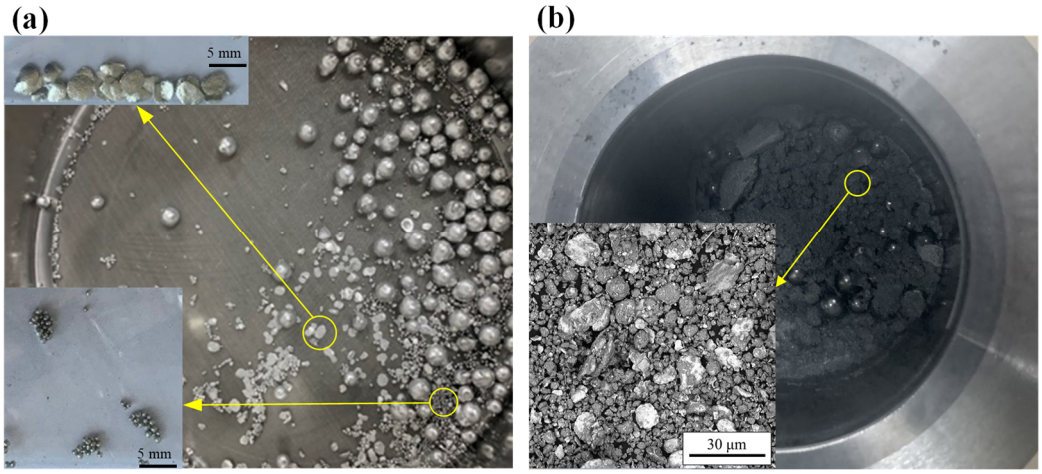

Figure 3. (**a**) Ball-milled powders without stearic acid with milling for 10 h; (**b**) Ball-milled powders after adding 2 wt.% stearic acid with milling for 10 h.

Figure 3b shows Ti and Al ball-milled powders with 2 wt.% stearic acid. Compared with the ball-milled powders without stearic acid, the inner wall of the milling vial with stearic acid was smooth, the grinding balls were bright, and there was no attachment. This is because stearic acid acts as a surfactant in powders during the ball-milling process, which effectively reduces the surface energy of the refined powder and avoids excessive cold welding of TiAl ball-milled powders. As shown in Figure 3b, the SEM morphology of mixed Ti and Al powders obtained after 10 h of ball milling presents spherical and ellipsoidal shapes, with powder sizes ranging from 2 μm to 18 μm, resulting in significant refinement. Powders with smaller particle sizes are mostly nearly spherical, while those with larger sizes are nearly ellipsoidal, and the overall size is relatively uniform. However, there are also larger spherical powders formed by bonding smaller-diameter powders. In addition, there are also flake-shaped powders and small powder shapes that fold and wrap around them. At this point, the number of small-sized Ti and Al powder particles significantly increase and the size becomes more uniform, indicating that during the ball-milling process, the degree of powder cold welding and crushing reaches equilibrium.

3.2. Reaction Mechanism of (Ti_2AlC + Al_2O_3)p/TiAl Composites

Figure 4 shows the XRD patterns of (Ti_2AlC + Al_2O_3)$_p$/TiAl composites prepared by adding different mass fractions of stearic acid (0 wt.%, 1 wt.%, 2 wt.%, and 3 wt.%) during the ball-milling process. Without adding stearic acid (0 wt.%), the as-prepared composites only contained γ-TiAl and α_2-Ti_3Al phases. For adding stearic acid (1 wt.%, 2 wt.%, and 3 wt.%) during the ball-milling process, the as-prepared composites were composed of γ-TiAl, α_2-Ti_3Al, Ti_2AlC, and Al_2O_3 phases. The reason for the formation of the Ti_2AlC and Al_2O_3 phases is that the C and O elements in the stearic acid were introduced into the TiAl ball-milled powders by mechanical ball milling to form the Ti-Al-C-O system, and the relevant reaction occurred during the subsequent sintering process to form the Ti_2AlC and Al_2O_3 phases. Meanwhile, it should be noted that the Ti_2AlC content increased with the increase in stearic acid content. Through semi-quantitative calculation using Highscore 5.1 software, the mass fractions of Ti_2AlC in the TiAl composites prepared by adding 1 wt.%, 2 wt.%, and 3 wt.% stearic acid were 4%, 7%, and 11%, respectively.

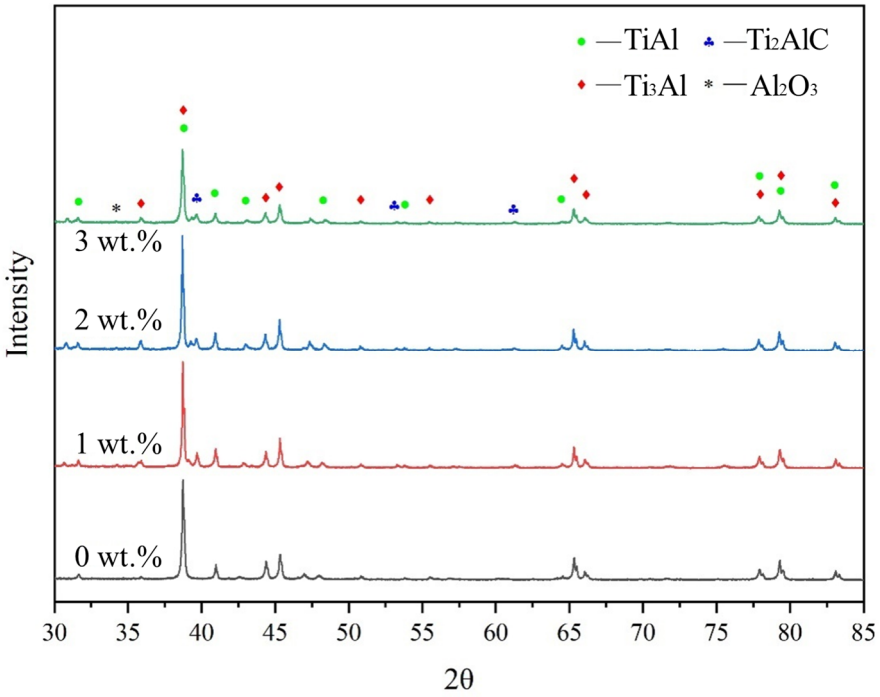

Figure 4. The XRD patterns of (Ti_2AlC + Al_2O_3)$_p$/TiAl composites prepared by adding different contents of stearic acid (0 wt.%, 1 wt.%, 2 wt.%, and 3 wt.%).

In order to further reveal the reaction mechanism of (Ti_2AlC + Al_2O_3)$_p$/TiAl composites, TG-DSC analysis was carried out on TiAl ball-milled powders with 2 wt.% of stearic acid, as shown in Figure 5. The DSC curve showed that there were two endothermic peaks and two exothermic peaks: when the temperature rose to around 580 °C, a relatively weak endothermic peak was observed; when the temperature reached around 660 °C, the second significant endothermic peak was observed. The first significant exothermic peak was observed when the temperature rose to 700 °C. After that, a less obvious exothermic peak appeared near 900 °C.

During the ball-milling process, the added stearic acid was decomposed, and C, H, and O elements were solidly dissolved in the lattice of Ti (Al) and formed intermediate TiH_2 [31]. At around 580 °C, the intermediate TiH_2 underwent thermal decomposition (as shown in reaction (2)), which was an endothermic reaction. So, the first weak endothermic peak around 580 °C occurred in the DSC curve.

$$TiH_2 \rightarrow Ti + H_2 (\uparrow) \quad (2)$$

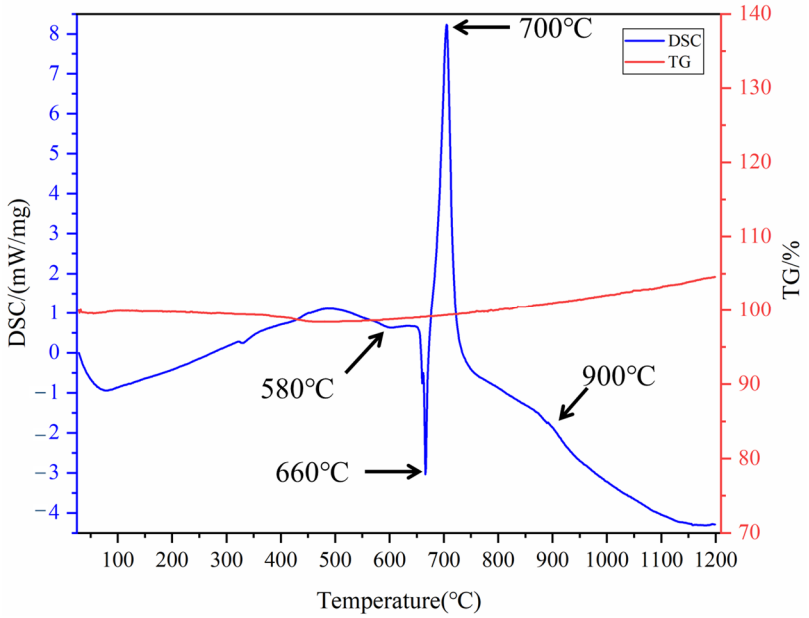

Figure 5. The TG-DSC curves of TiAl ball-milled powders with 2 wt.% of stearic acid.

The second endothermic peak at 660 °C was attributed to the melting of Al. The melting process of Al absorbed a mass of heat and formed the evident endothermic peak. While the exothermic peak appeared at 700 °C, it was mainly contributed to by the formation of TiAl intermetallic compounds. The formation of TiAl intermetallic compounds can be divided into two stages. One was the solid–solid diffusion reaction that occurred at a temperature lower than the melting point of Al. In this stage, the reaction rate of TiAl elements was very slow, and no obvious exothermic peak formed. The other was the liquid–solid reaction that occurred at a temperature higher than the melting point of Al. The melting of Al could effectively increase the reaction rate of Ti and Al atoms, which released a large amount of heat and formed the exothermic peak at 700 °C (reactions (3) and (4)).

In addition, the C and O elements decomposed by stearic acid were introduced into the TiAl reaction system and participated in the reactions (5) and (6) to generate TiC and Al_4C_3 [32]. As an intermediate phase, TiC also participated in the reaction of Ti_2AlC formation, as shown in reaction (8). However, due to the low C content, the heat released by these reactions (reactions (5), (6), and (8)) was limited. The exothermic peak at 700 °C was mainly contributed to by reactions (3) and (4). The exothermic peak at 900 °C was attributed to the reaction of Al_4C_3 with Al_3Ti, as shown in reaction (7). The exothermic peak at 900 °C was not very obvious due to the low content of the product Al_4C_3 and the less exothermic reaction.

$$Ti(s) + Al(s) \rightarrow TiAl_3(s) \quad (3)$$

$$TiAl_3(s) + Ti(s) \rightarrow TiAl(s) + Ti_3Al(s) \quad (4)$$

$$TiAl_3(s) + C(s) \rightarrow TiC(s) + Al(l) \quad (5)$$

$$Al + C \rightarrow Al_4C_3 \quad (6)$$

$$Al_4C_3(s) + TiAl_3(s) \rightarrow TiC(s) + Al(l) \quad (7)$$

$$TiC(s) + TiAl(s) \rightarrow Ti_2AlC(s) \quad (8)$$

3.3. Microstructure of (Ti_2AlC + Al_2O_3)p/TiAl Composites

Figure 6 shows the SEM morphologies of $(Ti_2AlC + Al_2O_3)_p$/TiAl composites prepared by adding different mass fractions of stearic acid (0 wt.%, 1 wt.%, 2 wt.%, and 3 wt.%). In Figure 6a, the microstructure of the sample without added stearic acid was mainly composed of dark gray and light gray phases. The light gray phase dispersed into the dark

gray phase, which exhibited a round or oval shape and an uneven morphology in size. According to the XRD patterns of the sample without added stearic acid in Figure 4, the material was mainly composed of γ-TiAl and α_2-Ti_3Al phases. EDS point scanning was performed on points 1 and 2 in Figure 6a, as shown in Table 2. The atomic ratio of Ti:Al at point 1 was close to 1:1, indicating that the dark gray was γ-TiAl. The Ti:Al atomic ratio at point 2 was close to 3:1, and the light gray was identified as α_2-Ti_3Al. In the process of preparing samples of $(Ti_2AlC + Al_2O_3)_p$/TiAl composites, the powder used for sintering was packaged with graphite paper in the mold, which caused C and O elements to infiltrate. This resulted in the sample containing carbon and oxygen elements without added stearic acid, and EDS point scan results showed high C and O content. The results of EDS were in agreement with the analysis of XRD. In addition, there were some holes in the selected district (delineated by the red line in Figure 6a). This was caused by the severe cold welding of TiAl powders. In addition, the TiAl mixing powders without added stearic acid must be milled at a slow revolving speed with a short milling time, so the TiAl ball-milled powders were not fully refined, and the size of the powder particles was not uniform, which led to the formation of a sintering neck.

Table 2. The results of EDS of point 1–3.

Element\at%	Point 1	Point 2	Point 3
Ti	43.6%	60.1%	43.2%
Al	41.6%	23.8%	28.1%
C	12.6%	10.2%	20.2%
O	2.2%	5.9%	8.5%

Figure 6b–d show the microstructures of $(Ti_2AlC + Al_2O_3)_p$/TiAl composites prepared by adding 1 wt.%, 2 wt.%, and 3 wt.% stearic acid, respectively. Compared with the sample without added stearic acid, in the $(Ti_2AlC + Al_2O_3)_p$/TiAl composites (in Figure 6b–d), a large number of white granular substances was also observed, besides the dark gray TiAl phase and light gray Ti_3Al phase. Through EDS point scanning at point 3 in Figure 6c, the atomic ratio of Ti:Al:C was close to 2:1:1 (as shown in Table 2). Combined with the XRD patterns in Figure 4, it can be determined that the white granular phase was MAX phase Ti_2AlC. Ti_2AlC particles were mainly located at the grain boundary of the TiAl matrix, and most of them were distributed in chain forms. In addition, a few Ti_2AlC particles were distributed at the TiAl/Ti_3Al interface and in the Ti_3Al phase, and there were several Ti_2AlC particles with a relatively larger size (Figure 6b,c).

In addition to Ti_2AlC particles (white particles), some black particles (indicated by the red arrows in Figure 6b) were also found attached to the chain-distributed Ti_2AlC enhancement phase. To determine the composition of the black particles, EDS surface scanning was performed on selected area I in Figure 6c, as shown in Figure 6f–i. It can be observed that the Ti-rich region in Figure 6f and the Al-poor region in Figure 6g corresponded to the Ti_3Al phase in Figure 6e. The distribution of C elements in Figure 6h was lower than that of Ti and Al, while the C-rich region corresponded to the distribution of the Ti_2AlC phase in Figure 6e. It can be seen from the distribution of the O element in Figure 6i that the content of O was less than that of C, and the O-rich regions exhibited a discrete distribution, which corresponded to the black particles in Figure 6e one by one. By combining the phase results of Figure 6e and the XRD results, it could be concluded that the O-rich black particles were Al_2O_3.

By comparing Figure 6b–d, it was found that as the content of stearic acid increased from 1 wt.% to 3 wt.%, the Ti_2AlC particles with chain-like distribution gradually connected to each other and thickened in width, as shown in the yellow area of Figure 6d. Moreover, the grain size of Ti_2AlC particles with chain-like distribution increased, with a chain length of about 20 μm and a width of about 3 μm.

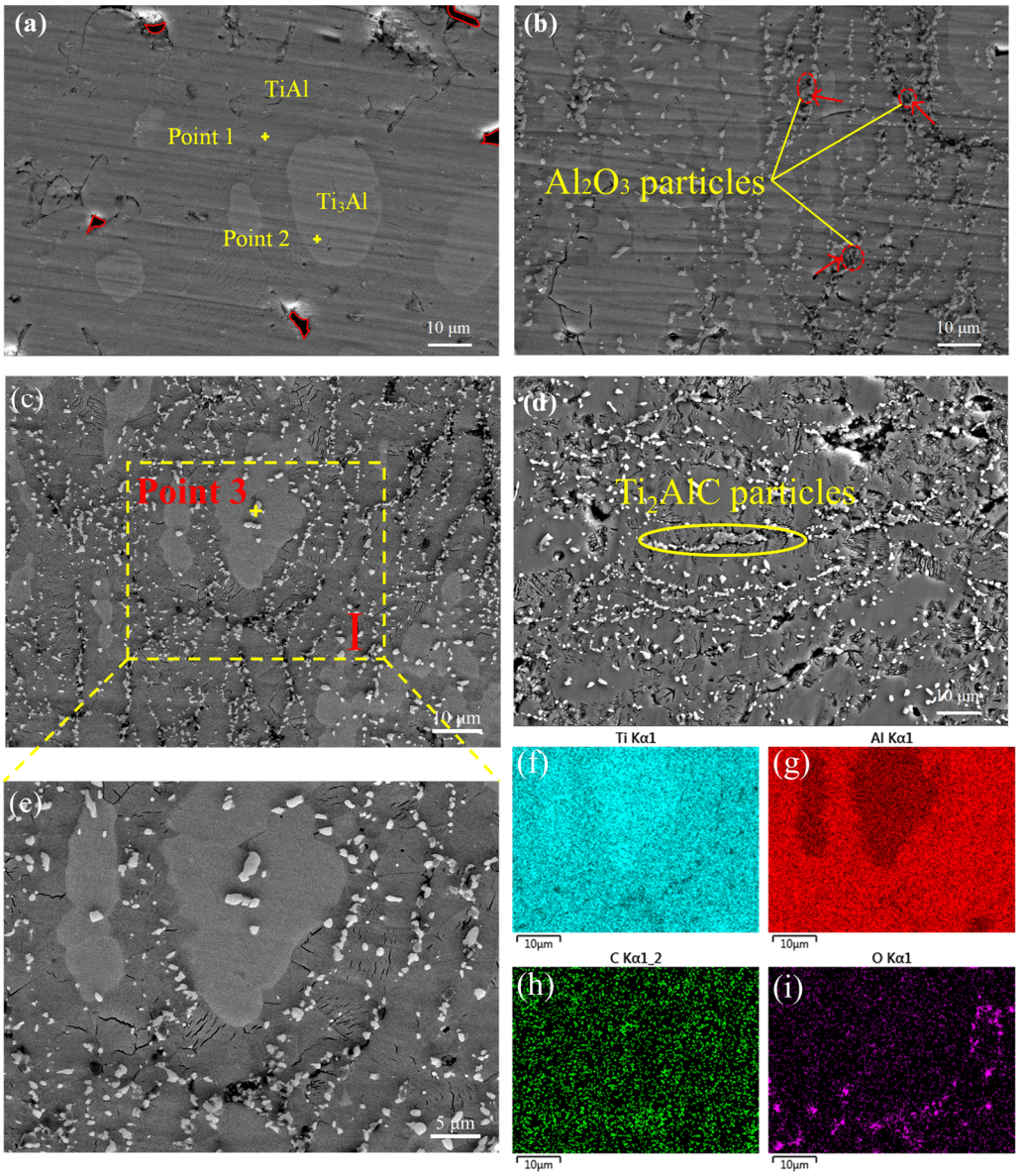

Figure 6. The SEM morphology of $(Ti_2AlC + Al_2O_3)_p$/TiAl composites prepared by adding (**a**) 0 wt.%, (**b**) 1 wt.%, (**c**) 2 wt.%, and (**d**) 3 wt.% stearic acid, respectively. (**e**) The enlarged image of selection I in the sample with 2 wt.% steric acid, and (**f**–**i**) is the EDS element maps of selection I aera.

Figure 7a,b show the fracture morphology of the composites without added stearic acid and $(Ti_2AlC + Al_2O_3)_p$/TiAl composites, respectively. It was found that a higher amount of refined TiAl grains appeared in $(Ti_2AlC + Al_2O_3)_p$/TiAl composites compared with the additive-free sample. The reason is that the chain-form distribution of Ti_2AlC and Al_2O_3 particles hindered the diffusion of Ti and Al atoms and effectively limited the growth of TiAl grains. Additionally, combined with Figure 7c,d, it can be found that the Ti_3Al grains are bigger than the TiAl grains, and the closer the TiAl grains are to the chain distribution of Ti_2AlC and Al_2O_3 particles, the more refined the TiAl grains.

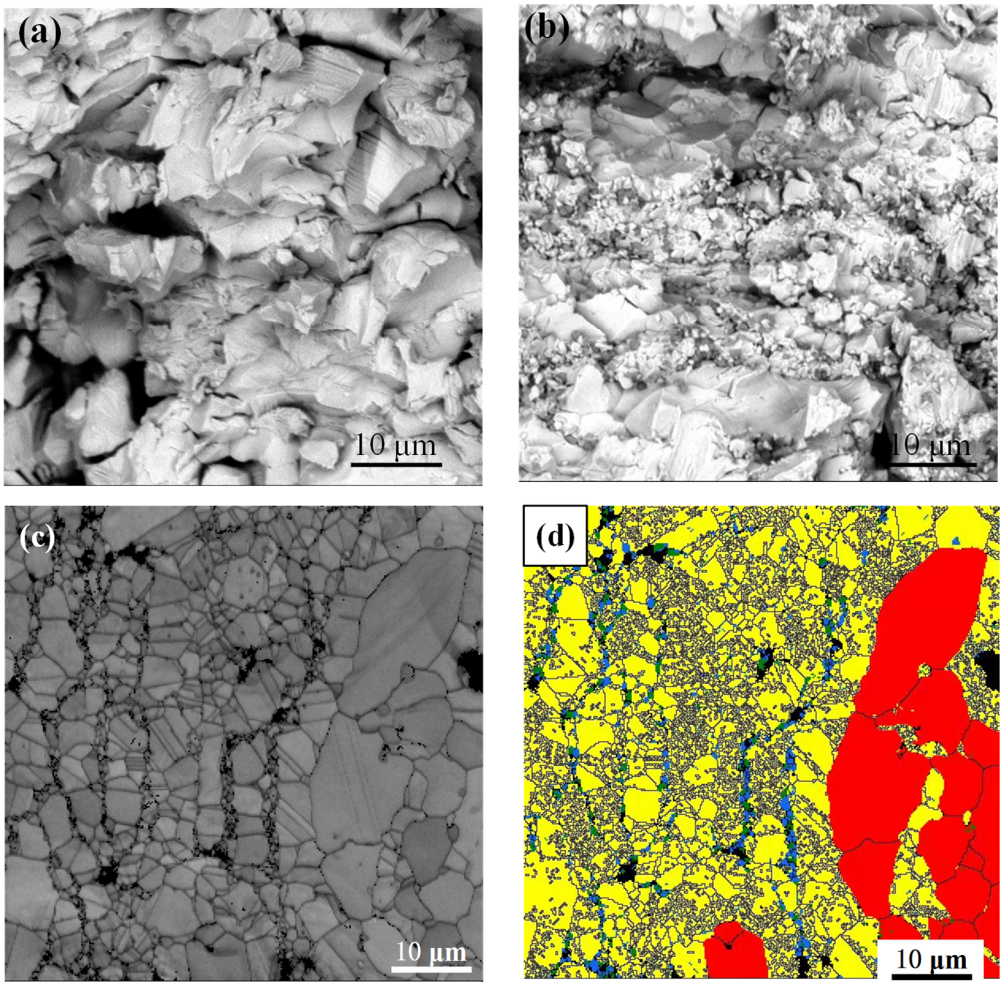

Figure 7. Fracture morphology of $(Ti_2AlC + Al_2O_3)_p/TiAl$ composites prepared by adding different mass fractions ((**a**) 0 wt.% and (**b**) 1 wt.%) of stearic acid under room-temperature compression failure; (**c**) band contrast map and (**d**) phase contrast map of $(Ti_2AlC + Al_2O_3)_p/TiAl$ composites (yellow represents TiAl grains, red represents Ti_3Al grains, blue represents Ti_2AlC grains, and green represents Al_2O_3 grains).

Figure 8a shows the TEM morphology of $(Ti_2AlC + Al_2O_3)_p/TiAl$ composites prepared by adding 2 wt.% stearic acid during the ball-milling process. It can be seen in Figure 8a that there is a small amount of γ/α_2 lamellar in $(Ti_2AlC + Al_2O_3)_p/TiAl$ composites. The formation of γ/α_2 lamellar can be attributed to the exothermic reaction between Ti and Al during the sintering process.

As the DSC curve in Figure 5 shows, with the melting of Al, the liquid Al can effectively increase the reaction rate of Ti and Al atoms, which releases a large amount of heat and produces a high temperature that may reach the α phase region in the local area. With the end of the exothermic reaction of TiAl intermetallic, the temperature is gradually consistent with the temperature of the furnace, and it is stable in the $(\alpha + \gamma)$ phase region. When the material is kept at the temperature of the $(\gamma + \alpha)$ phase region for a certain time, the newly formed equiaxed γ phase will be transformed into more stable γ/α_2 lamellar aggregates. In addition, in Figure 8a, the twin structures (indicated by the yellow arrows) are observed, and the HRTEM image of the γ/γ twin boundary is shown in Figure 8c. The selected electron diffraction patterns of the yellow dotted circle in Figure 8a are shown in Figure 8d. In Figure 8c, it can be seen that the TiAl diffraction lattice has different orientations. According to the SAED of the γ/γ twin boundary, it can be noted that the direction is the axis of symmetry, with a 60° mirror symmetry. The formation of twin structures in the γ-TiAl phase is mainly attributed to the hot deformation in the process of

sintering. In this paper, in order to obtain dense composites, when the sintering temperature rises to 1150 °C, the composites will suffer from pressure from the liquid head. Under this condition, the dislocation at the TiAl grain boundaries forms, as shown in Figure 8b. Due to the absence of a slip system for γ-TiAl, the interface dislocation can only move along the interface; when the dislocation stacking structure is formed, it is difficult to remove. As local stress concentrates, the dislocations will enter γ grains and form deformation twins.

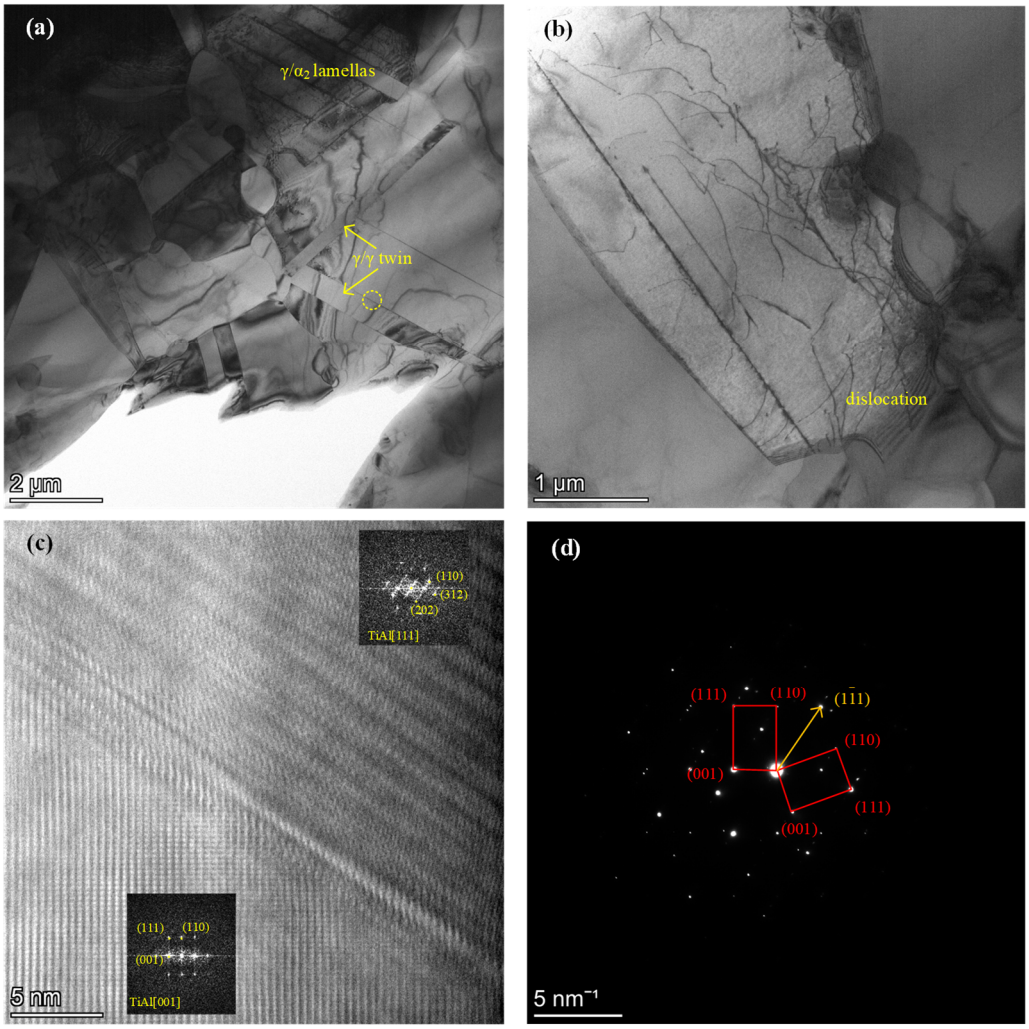

Figure 8. $(Ti_2AlC + Al_2O_3)_p$/TiAl composites prepared by adding 2 wt.% stearic acid. (**a**) TEM morphology; (**b**) dislocation of γ grain; (**c**) HRTEM image of boundary of γ/γ twin; (**d**) SAED selected pattern of yellow dotted line in (**a**) aera.

Figure 9 shows the TEM diagram of $(Ti_2AlC + Al_2O_3)_p$/TiAl composites. It can be seen in Figure 9a that there are several dark- and light-enhanced particles on the TiAl matrix. When the sintering temperature is within the range of 900–1200 °C, the prepared $(Ti_2AlC + Al_2O_3)_p$/TiAl composite matrix is mainly composed of equiaxed TiAl and Ti_3Al two-phase structures—1–5 enhanced particles, respectively. In order to determine the element distribution, EDX analysis was performed on the selected region in the yellow rectangular box area in Figure 9b, and the results of the EDX are shown in Figure 9c–f. Combined with Figure 9a,c–f, it can be noticed that the No. 2, 4, and 5 particles are poor in Ti and C elements. In contrast, the Al and O elements are abundant in these regions. O elements, especially, are mainly enriched in the corresponding regions of No. 2, 4, and 5 particles and basically have no distribution in other locations. The point scanning analysis of the No. 2 particle shows that the atomic content of Al and O is 38.76% and 61.24%, respectively, and the atomic ratio is approximately 3:2. Therefore, it can be determined

that the No. 2, 4, and 5 particles with a lighter color are Al_2O_3 particles. Dark particles No. 1 and 3 are mainly rich in the Ti/C region. Combined with the analysis in the previous section, the No. 1 and 3 particles are Ti_2AlC particles. Based on the above analysis, it can be found that Ti_2AlC and Al_2O_3 particles are alternately distributed at the TiAl grain boundary. In addition, there are pores in the center of the region surrounded by 1—Ti_2AlC, 2—Al_2O_3, 3—Ti_2AlC, and 4—Al_2O_3 grains, as shown in the red area in Figure 9b. This is because Ti_2AlC + Al_2O_3-reinforced particles inhibit the diffusion of TiAl elements, and there is no matrix formation in these aggregate areas, resulting in pores. This also explains the large number of pores in the TiAl composite with 3 wt.% stearic acid additions. The porosity of $(Ti_2AlC\text{-}Al_2O_3)_p$/TiAl composites is unfavorable to improving the density and mechanical properties.

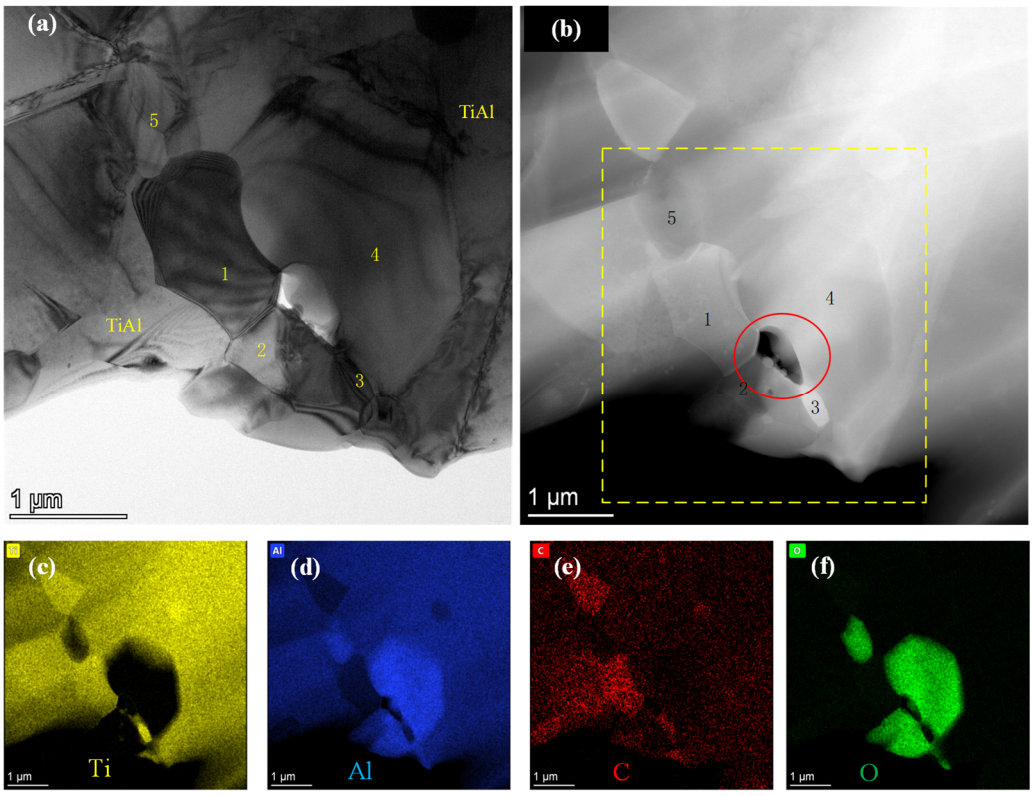

Figure 9. (Ti_2AlC + Al_2O_3)$_p$/TiAl composites (with 2 wt.% stearic acid added during ball milling, prepared by sintering at 1150 °C): (**a**) BF-TEM image; (**b**) HAADF-SETM image; (**c**–**f**) EDX element distribution diagram in the yellow rectangular box area in (**b**), corresponding to Ti, Al, C, and O elements, respectively.

Figure 10a,b are HRTEM images of the Ti_2AlC/TiAl interface and the Al_2O_3/TiAl interface, respectively. In Figure 10a, the upper part is Ti_2AlC; the crystal plane spacing of Ti_2AlC-(101) is 0.2589 nm; the lower part is TiAl; and the crystal plane spacing of TiAl-(002) is 0.2078 nm. In Figure 10b, the upper left part is TiAl; the measured TiAl-(101) crystal plane spacing is 0.2344 nm; the lower part is Al_2O_3; the measured crystal plane spacing of Al_2O_3-(202) is 0.2381 nm. The FFT image of the Ti_2AlC/TiAl interface that is marked by a red dashed rectangle is shown in Figure 10c. It can be noticed that the TiAl-(110)//Ti_2AlC-(101). This orientation between TiAl and Ti_2AlC makes the bonding of Ti_2AlC at the interface of the TiAl matrix more stable [33]. Additionally, the IFFT image of the TiAl(002) and TiAl-($00\bar{2}$) planes is shown in Figure 10e, where the TiAl is close to Ti_2AlC. It can be seen that there are few dislocations in the TiAl grains at the Ti_2AlC/TiAl interface in Figure 10e, while, for the FFT image of the TiAl/Al_2O_3 interface, there is a slight deflection between Al_2O_3-(207) and TiAl-(002) (as shown in Figure 10d). Cui et al. [34]

referred to the Al_2O_3-(006)//TiAl-(111), which exhibits a coherent relationship. Thus, the interface between Al_2O_3 and TiAl is bounding well. However, compared with the IFFT images of the TiAl-(002) and TiAl-(00$\bar{2}$) planes in Figure 10f, where the TiAl is close to Al_2O_3, it can be found that a large number of dislocations are located at the TiAl matrix near Al_2O_3, and the closer TiAl is to Al_2O_3, the higher the dislocation density is. This phenomenon means that when the material is subjected to external loading, compared with the "soft" Ti_2AlC-enhanced phase, the Al_2O_3 particles have a stronger ability to anchor the dislocation in the TiAl matrix. The same phenomenon was observed by Cui et al. [35]. They found that a mass of dislocations was stored in the TiAl matrix near the Mo_2B_5 nanoparticle region, which proves the pinning effect of Mo_2B_5 particles on dislocations was stronger than that of Ti_2AlC particles.

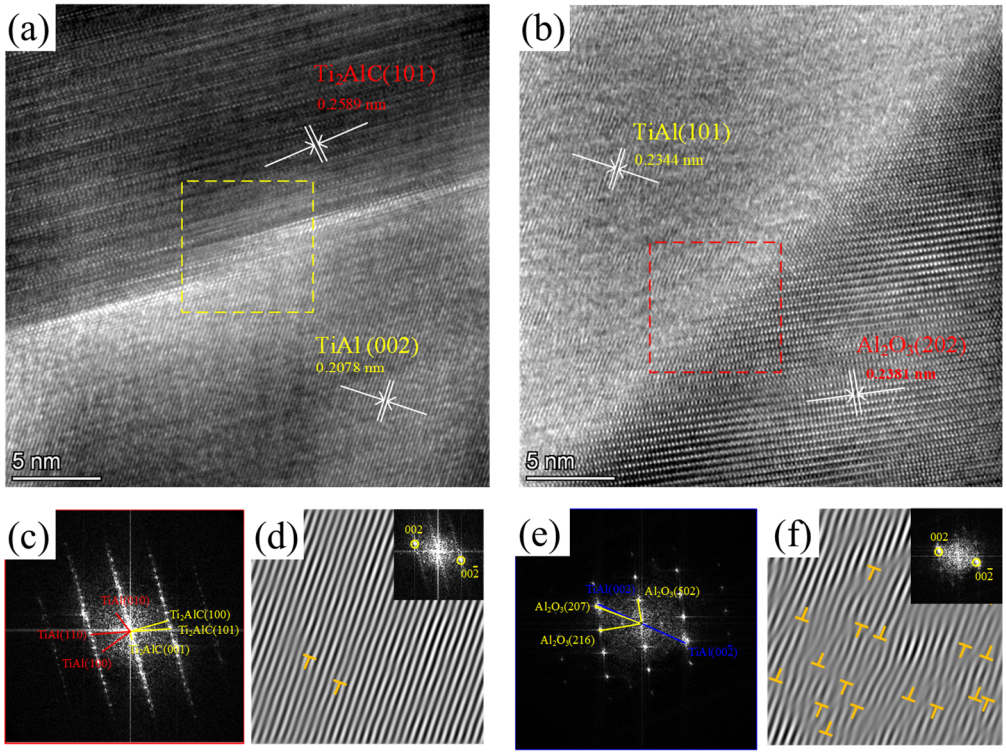

Figure 10. $(Ti_2AlC + Al_2O_3)_p$/TiAl composites (with 2 wt.% stearic acid added during ball milling, prepared by sintering at 1150 °C): (**a**) HRTEM image of Ti_2AlC/TiAl interface; (**b**) HRTEM image of Al_2O_3/TiAl interface; (**c**) FFT image of Ti_2AlC/TiAl interface; (**d**) IFFT image of TiAl close to Ti_2AlC; (**e**) FFT Image of Al_2O_3/TiAl interface; (**f**) IFFT image of TiAl close to Al_2O_3.

3.4. Mechanical Properties of $(Ti_2AlC + Al_2O_3)p$/TiAl Composites

Figure 11 shows the microhardness of the sample without added stearic acid and $(Ti_2AlC + Al_2O_3)_p$/TiAl composites prepared by adding 1 wt.%, 2 wt.%, and 3 wt.% stearic acid during the ball-milling process at a sintering temperature of 1150 °C. As seen in Figure 11, the hardness of the sample without added stearic acid is the lowest, and its microhardness is 2.8 GPa. For the microhardness of $(Ti_2AlC + Al_2O_3)_p$/TiAl composites, meanwhile, the microhardness increases firstly and then decreases with the increase of stearic acid addition. The maximum microhardness of the $(Ti_2AlC + Al_2O_3)_p$/TiAl composite prepared by adding 2 wt.% stearic acid is 7.7 GPa. However, when the additive dosage of stearic acid is 3 wt.%, the hardness decreases.

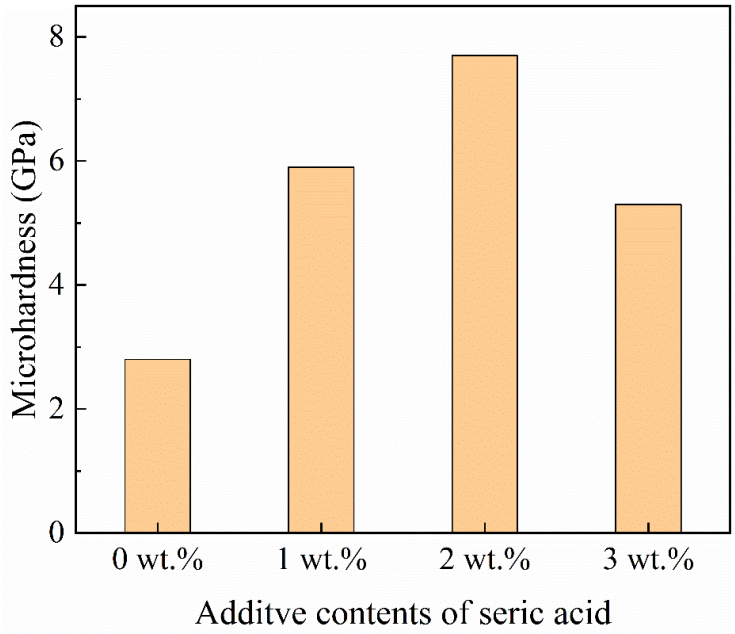

Figure 11. Microhardness of $(Ti_2AlC + Al_2O_3)_p$/TiAl composites prepared with different stearic acid additions.

It is found that the microhardness of $(Ti_2AlC + Al_2O_3)_p$/TiAl composites prepared with stearic acid is significantly higher than that of the additive-free samples. This is due to the formation of Ti_2AlC- and Al_2O_3-reinforced particles during the sintering process by trace C and O elements introduced by stearic acid during ball milling, as described in Section 3.4. Firstly, the distribution of Ti_2AlC- and Al_2O_3-reinforced particles is mainly located at the TiAl grain boundary, which refines the TiAl grains and improves the microhardness of the material. Secondly, compared with the microhardness of the additive-free sample, the microhardness of Ti_2AlC and Al_2O_3 as reinforcement phases is 4.5 GPa [36] and 9 GPa [30], respectively, which are higher than that of TiAl (3.15 GPa [37]). In certain content ranges, with the volume fraction of the reinforcement particles Ti_2AlC and Al_2O_3 increasing, the overall microhardness of the composites is improved through the synergistic effect. However, as discussed in Section 3.2, when the added amount of stearic acid reaches 3 wt.%, the introduction of C and O elements further increases the content of composites, and the content of Ti_2AlC and Al_2O_3 increases, which makes it easier to form reinforced particle aggregates and the formation of voids in the intersections of TiAl grain boundaries where the reinforced particles are located, which will lead to a decrease in the density of composites. Thus, for the $(Ti_2AlC + Al_2O_3)_p$/TiAl composite with 3 wt.% stearic acid added, the microhardness decreases but is still higher than that of the sample without stearic acid during the ball-milling process.

Cheng et al. [21] prepared near-mesh Ti_2AlC-reinforced TiAl matrix composites and found that the hardness also increased with the increase of Ti_2AlC content, with a maximum hardness of 6.46 GPa. Lu et al. [30] prepared Al_2O_3/TiAl composites by the hot-pressing method and found that the yield strength and hardness of Al_2O_3/TiAl composites also improved with the increase in Al_2O_3 content. Its maximum hardness reaches 4.126 GPa. Compared with the microhardness of the composite materials prepared by Cheng et al. [21] and Lu et al. [30], it was found that the $(Ti_2AlC + Al_2O_3)_p$/TiAl composites were prepared in this study and had the highest hardnesses, which were 19.2% and 86.6% higher, respectively.

Figure 12 shows the room-temperature compressive stress–strain curves of $(Ti_2AlC + Al_2O_3)_p$/TiAl composites prepared by sintering at 1150 °C with different stearic acid additions. It can be seen in Figure 12 that the compressive properties of $(Ti_2AlC + Al_2O_3)_p$/TiAl composites are sensitive to the additive amount of stearic acid. The yield strength and maximum compressive strength of the composite increased with the increase in stearic acid content

from 0 wt.% to 2 wt.%. The composite prepared by adding 1 wt.% had similar compressive properties to that prepared by adding 2 wt.%, and the composite prepared by adding 1 wt.% had a higher yield strength. The maximum compressive strength and fracture strain were found in the 2 wt.% composites. However, the yield strength and maximum compressive strength of the $(Ti_2AlC + Al_2O_3)_p$/TiAl composites decreased when the addition of stearic acid increased by 3 wt.%. As shown in Table 3, the maximum compressive strength of the TiAl alloy and $(Ti_2AlC + Al_2O_3)_p$/TiAl composite prepared with 0 wt.%, 1 wt.%, 2 wt.%, and 3 wt.% stearic acid additions is 850 MPa, 1574 MPa, 1590 MPa, and 1234 MPa, respectively. The yield strengths are 266 MPa, 542 MPa, 538 MPa, and 464 MPa, respectively. When the strength is increased, the fracture strain is also increased and is 0.214, 0.231, 0.241, and 0.217, respectively.

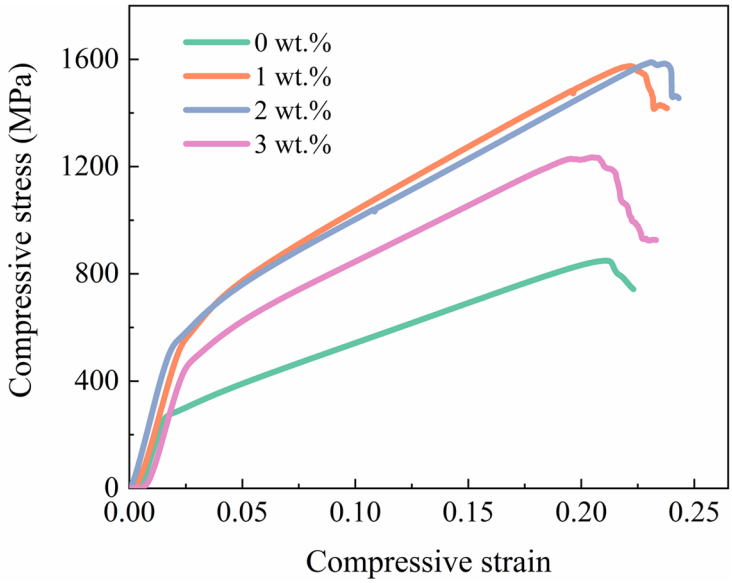

Figure 12. Compressive strain–stress curves of TiAl matrix composites with different addition amounts of stearic acid at room temperature.

Table 3. The room-temperature compression properties of $(Ti_2AlC + Al_2O_3)$p/TiAl composites prepared with different stearic acid addition.

Additive Content of Stearic Acid wt.%	σ_{cy} MPa	σ_{ucs} MPa	Strain
0	266	850	0.221
1	542	1574	0.238
2	538	1590	0.243
3	464	1234	0.223

It can be seen that the compressive properties of $(Ti_2AlC + Al_2O_3)_p$/TiAl composites at room temperature are closely related to the addition of stearic acid. As the amount of stearic acid added increases, the yield strength and maximum compressive strength of $(Ti_2AlC + Al_2O_3)_p$/TiAl composites also increase. Based on the research of Chen et al. [19] (Ti_2AlC/TiAl composites with WC particles added), Shu et al. [20] (Ti_2AlC/TiAl composites with Nb-C added), and Cheng et al. [21] (near-mesh Ti_2AlC-reinforced TiAl matrix composites with nano-TiC powder added), it was found that the room-temperature compressive strength and fracture strain of the prepared Ti_2AlC/TiAl composites increase with the increase of the content of additives as a carbon source (within a certain range). This indicates that Ti_2AlC particles have a significant enhancing effect on the mechanical properties of TiAl matrix composites, which is consistent with the results of this study.

The composite material prepared by adding 2 wt.% stearic acid has the maximum compressive strength, which is 1590 MPa. Compared to the sample without added stearic

acid, it increases by 87%. While ensuring strength, the fracture strain is also improved to a certain extent. The maximum fracture strain of the composite material prepared by adding 2 wt.% stearic acid reaches 0.241, which is 12.6% higher than that of the sample without stearic acid added. Compared with the compressive strength of the composite materials prepared by Shu et al. [20] and Cheng et al. [21], it is found that the maximum compressive strength of the $(Ti_2AlC + Al_2O_3)_p/TiAl$ composites prepared in this study under room-temperature compression testing (with the addition of 2 wt.% stearic acid) increase by 23% and 14%, respectively. Compared with the composite materials prepared by Chen et al. [19] and Shu et al. [20], the maximum fracture strain increased by 12% and 80%, respectively.

Through relevant research reports (TiAl alloys and single-phase reinforced TiAl matrix composites), as shown in Figure 13a, it was found that although the compressive strength of $Ti_2AlC/TiAl$ composites [38–42] (except for 0.5 wt.% Ti_2AlC/Ti48Al2Nb [23] and 5 wt.% $Ti_2AlC/TiAl$ (Nb-C) [20] in Figure 13a) was higher than that of this work, their fracture strains were all less than 0.2, indicating no significant improvement in toughness. Compared to $Ti_2AlC/TiAl$ composites, the compressive strength and fracture strain of $Al_2O_3/TiAl$ composites [30] are almost smaller. The room-temperature compressive strength of the TiAl alloy [37] did not exceed 1400 MPa, and the maximum fracture strain was only 0.05. It can be observed that the fracture strain of $(Ti_2AlC + Al_2O_3)_p/TiAl$ composites reinforced with multiphase nanoparticles far exceeds that of most TiAl alloys and TiAl matrix composites, while the compressive strength remains at a relatively high level. As shown in Figure 13b, the compressive stress–strain relationship of the $(Ti_2AlC + Al_2O_3)_p/TiAl$ composites studied in this work was compared with other TiAl matrix composites and TiAl alloys [23,30,37,40,43]. It could be seen that the compressive stress strain of $(Ti_2AlC + Al_2O_3)_p/TiAl$ composites far exceeded that of most TiAl alloys and TiAl matrix composites. The above results indicated that the multiphase nanoparticle-reinforced $(Ti_2AlC + Al_2O_3)_p/TiAl$ composites prepared in this study had excellent synergistic effects on strength and toughness.

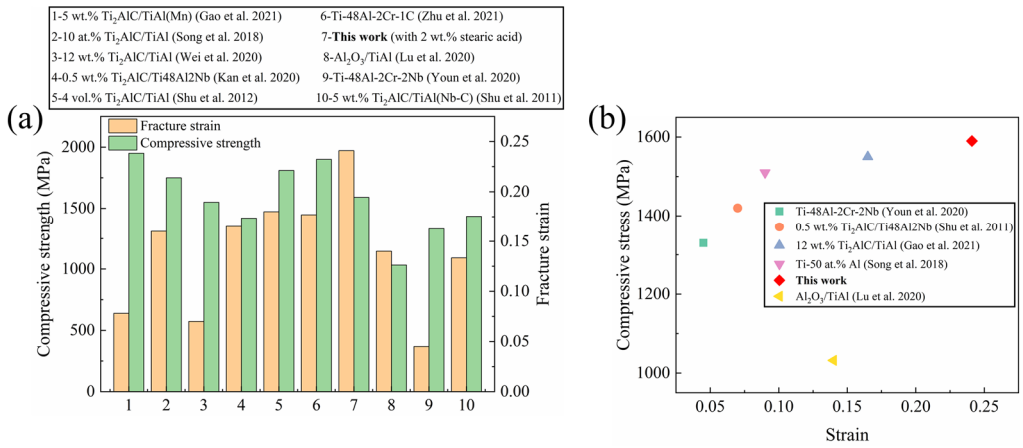

Figure 13. (**a**) Comparison of compressive strength and fracture strain of different TiAl matrix composites. (**b**) Compressive stress–strain relationship of different TiAl matrix composites [20,23,30,37–43].

The increase in strength is mainly due to the formation of Ti_2AlC and Al_2O_3 particles. On the one hand, Ti_2AlC and Al_2O_3 particles (the amount of stearic acid added is 1 wt.%, 2 wt.%, and 3 wt.%) are distributed in chain form at the grain boundaries of the TiAl matrix and Ti_3Al, which effectively inhibit grain growth and significantly refine the grain of the matrix. In addition, the mechanical high-energy ball-milling process has a certain effect on the refinement of the original TiAl mixture and the grain refinement of the subsequent sintered composites. On the other hand, as a hard ceramic phase, Al_2O_3 also plays an important role in improving the material strength of $(Ti_2AlC + Al_2O_3)_p/TiAl$ composites. The twin boundary in TiAl composites also improves strength. Vinogradov

et al. [44] verified that γ/γ twins promote the formation of dislocation bundles by hindering dislocation motion. High-density γ/γ twins lead to strain hardening of the additive-free sample. Therefore, the strength of a γ-TiAl-based alloy rich in twins can be enhanced by these twin grain boundaries. However, when the amount of stearic acid is 3 wt.%, the content of Ti_2AlC and Al_2O_3 increases, and the agglomeration of reinforced particles occurs at the intersection of chain distribution, which makes it easy to produce voids and other defects in the center of the mass. When the material is subjected to load, the crack source is first formed at the defect, accelerating the failure of the composites.

In addition, it can be seen in Figure 12 that the stress–strain curve of $(Ti_2AlC + Al_2O_3)_p/TiAl$ composites has obvious work hardening. According to Formula (9) [45], the work hardening capacity of the additive-free sample and $(Ti_2AlC + Al_2O_3)_p/TiAl$ composites can be calculated.

$$(\sigma_{ucs} - \sigma_{cy})/\sigma_{cy} \quad (9)$$

where σ_{ucs} is the maximum compressive strength of the material and σ_{cy} is the yield strength of the material. By calculation, the work-hardening capacity of the composite prepared by adding 0 wt.%, 1 wt.%, 2 wt.%, and 3 wt.% stearic acid is 2.19, 1.904, 1.95, and 1.65, respectively. It can be seen that, with the addition of stearic acid, the work-hardening ability of the $(Ti_2AlC + Al_2O_3)_p/TiAl$ alloy decreases compared with that of the additive-free sample without the reinforcing phase. This is due to the presence of Ti_2AlC and Al_2O_3 particles, which improve the yield strength of the TiAl composites. At the same time, they increase the critical starting stress of dislocation in the TiAl matrix and reduce the proliferation, accumulation, and interaction of dislocation in the hot deformation of the composites during sintering, resulting in the weakening of the work-hardening capacity.

Figure 14 shows the compressive failure morphology of TiAl composites at room temperature by adding different mass fractions (0 wt.%, 2 wt.%) of stearic acid during the ball-milling process. Figure 14a,b show the failure morphology of the sample without added stearic acid. It can be seen in Figure 14a that the fracture surface of TiAl is rough, indicating the shear force is small. According to Figure 14b, it can be concluded that the cleavage fracture is the main fault, with obvious intergranular and transgranular fractures. Additionally, as shown in the blue area in Figure 14b, the shear zone can also be observed, which is typical of brittle fracture characteristics. In addition, as shown in the yellow area, when the crack expands to the edge of the lamellar structure—due to the hinder of the local lamellar structure—the crack deflects and continues to expand along the edge of the lamellar structure, which increases the crack propagation path and improves the toughness to a certain extent.

Figure 14c,d show the failure morphology of $(Ti_2AlC + Al_2O_3)_p/TiAl$ composites prepared by adding 2 wt.% stearic acid. As seen in Figure 14c, the main crack of the sample begins to expand from the top of the sample. After a certain distance of expansion perpendicular to the section, it begins to rapidly expand along the direction of 45°, which belongs to the shear stress, leading to crack growth and failure. According to the $(Ti_2AlC + Al_2O_3)_p/TiAl$ composite compression failure morphology at room temperature with magnification in Figure 14d, complex mixed failure modes can be observed. The failure of the TiAl matrix is still typical of intergranular and transgranular fractures. In addition, it can be seen that the cracks spread along the $Ti_2AlC + Al_2O_3$ boundary of the TiAl matrix, and the cracks deflect at the reinforced particles. Meanwhile, the reinforced particles pull out, and pinning can also be found, both of which make the crack propagation path greatly increased, improving the TiAl composite's toughness.

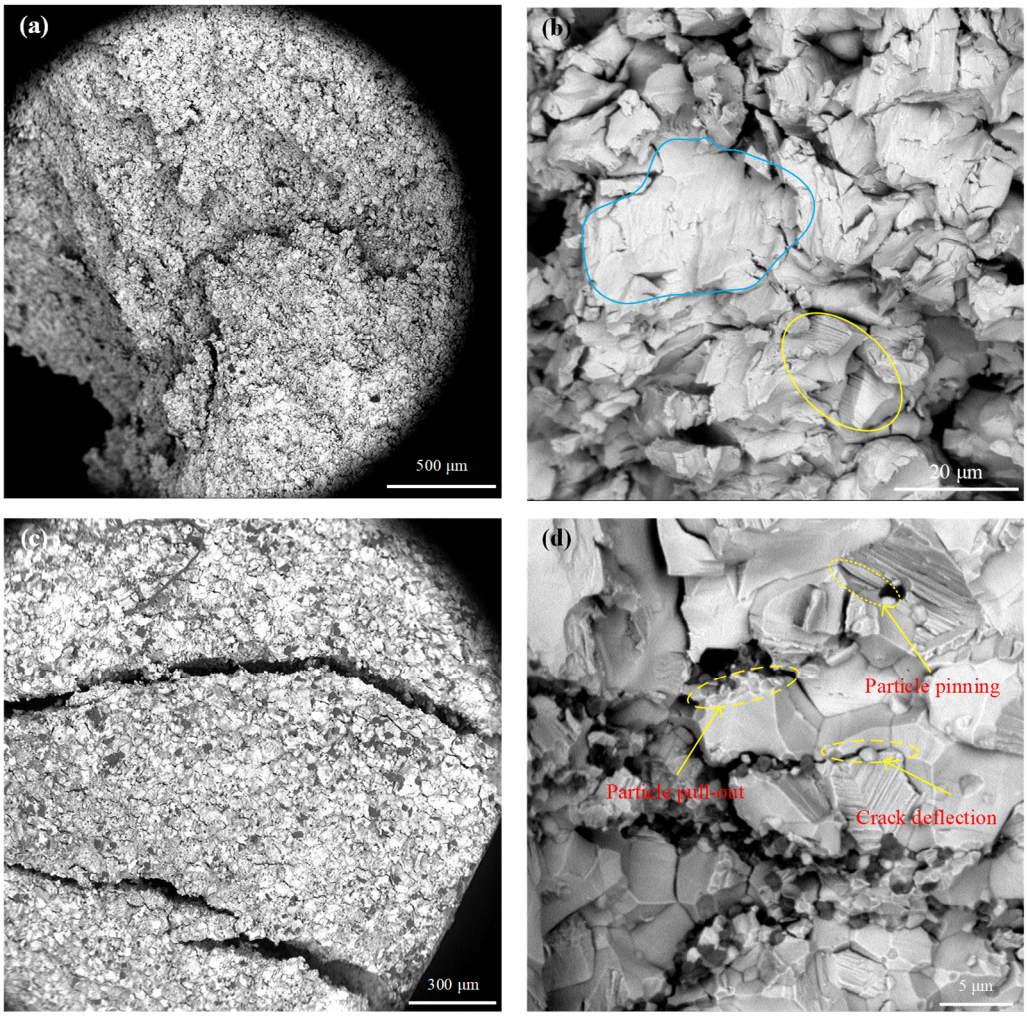

Figure 14. Failure morphology of $(Ti_2AlC + Al_2O_3)_p$/TiAl composites prepared with adding (**a**,**b**) 0 wt.%; (**c**,**d**) 2 wt.% stearic acid.

4. Conclusions

This study investigated the effects of stearic acid on the microstructure and mechanical properties of $(Ti_2AlC + Al_2O_3)_p$/TiAl composites fabricated by ball milling and vacuum hot-pressing sintering. Different additive amounts of stearic acid were used in the ball-milling process. At this stage, the stearic acid acted, and $(Ti_2AlC + Al_2O_3)_p$/TiAl composites were successfully fabricated by vacuum hot-pressing sintering by ball-milling mixed powders with stearic acid. In this stage, the stearic acid acted as the C and O element resources to facilitate the formation of Ti_2AlC and Al_2O_3. Several conclusions drawn from this research are summarized as follows:

(1) When the ball-milling powder is milled without adding stearic acid, resulting from severe cold welding of ductile Al powder, the ball-milled product adheres to the surface of the milling vial and grinding balls. With the stearic acid added initially, the powder yields nearly 100%.

(2) The TG-DSC and XRD curves indicate that the C and O elements of stearic acid participate in the TiAl reaction system, and the H element of stearic acid is involved in $H_2\uparrow$ release during the sintering process. And for the sample without added stearic acid, the XRD patterns only consist of the γ-TiAl phase and the α_2-Ti_3Al phase. While, for the composites that added stearic acid as a process control agent in the ball-milling process, the Ti_2AlC and Al_2O_3 patterns appear besides the γ-TiAl and α_2-Ti_3Al patterns.

(3) The microstructure of TiAl composites is mainly composed of equiaxed TiAl and Ti_3Al grains. While for the TiAl composites with stearic acid, the Ti_2AlC and Al_2O_3 particles are distributed at TiAl grain boundaries, a few Ti_2AlC particles are distributed at the TiAl/Ti_3Al interface and in the Ti_3Al phase. Additionally, γ/α_2 lamellar and γ/γ twin grains can be found in the TEM result.

(4) With the addition of stearic acid, the microhardness, the compression stress, and the fracture strain increase first and then decrease. The composite with the best comprehensive mechanical properties is $(Ti_2AlC + Al_2O_3)_p$/TiAl composite with 2 wt.% stearic acid; the microhardness, the compression stress, and the fracture strain are 7.7 GPa, 1590 MPa, and 24.3%. The improved strength of the TiAl composites results from refined TiAl grains and twin grain boundaries; the improved toughness is mainly caused by crack deflection, reinforced particle pull-out, and pinning.

Author Contributions: Conceptualization, methodology, and software, J.Z.; validation, J.Z. and M.Y.; formal analysis, M.Y.; investigation and resources, X.P. and X.Z.; data curation, J.Z. and X.Z.; writing—original draft preparation, J.Z.; writing—review and editing, M.Y.; visualization and supervision, X.P. and M.L.; project administration, X.Z.; funding acquisition, M.L. All authors have read and agreed to the published version of the manuscript.

Funding: This research was funded by the National Natural Science Foundation of China (51201155), the Natural Science Foundation of Shanxi Province, China (202203021222074, 20210302124213, 2012011019-1, 2012011007-1), the Specialized Research Fund for the Doctoral Program of Higher Education (20101420120006), the National Key Research and Development Plan of China (2018YFC1901704), and rapid support from the Science and Technology Committee of the Military Commission (80923010403).

Data Availability Statement: The raw/processed data required to reproduce these findings cannot be shared at this time due to technical and time limitations.

Conflicts of Interest: We declare that we have no financial and personal relationships with other people or organizations that can influence our work submitted in the manuscript entitled "The effect of stearic acid on microstructure and properties of $(Ti_2AlC + Al_2O_3)_p$/TiAl composites". Meanwhile, the submitted manuscript is approved for publication by all authors. The funders had no role in the design of the study; in the collection, analyses, or interpretation of data; in the writing of the manuscript; or in the decision to publish the results.

References

1. Chen, Y.; Cao, Y.; Qi, Z.; Chen, G. Increasing high-temperature fatigue resistance of polysynthetic twinned TiAl single crystal by plastic strain delocalization. *J. Mater. Sci. Technol.* **2021**, *93*, 53–59. [CrossRef]
2. Genc, O.; Unal, R. Development of gamma titanium aluminide (γ-TiAl) alloys: A review. *J. Alloys Compd.* **2022**, *929*, 167262. [CrossRef]
3. Kim, J.Y.; Park, E.S.; Lee, T.; Ryu, S.; Kim, S.-E.; Kim, S.-W. Origin of enhanced room temperature ductility in TiAl alloys: Reducing activation difference of deformation mechanism of γ phase. *J. Alloys Compd.* **2022**, *899*, 163307. [CrossRef]
4. Selvarajou, B.; Jhon, M.H.; Ramanujan, R.V.; Quek, S.S. Temperature dependent anisotropic mechanical behavior of TiAl based alloys. *Int. J. Plast.* **2022**, *152*, 103175. [CrossRef]
5. Yue, X.A.; Shen, J.; Xiong, Y.; Zheng, S. Microstructure control and mechanical properties of directionally solidified large size TiAl alloy by electromagnetic confinement. *Intermetallics* **2022**, *140*, 107406. [CrossRef]
6. Lu, K.; Lu, L.; Suresh, S. Strengthening Materials by Engineering Coherent Internal Boundaries at the Nanoscale. *Science* **2009**, *324*, 349–352. [CrossRef] [PubMed]
7. He, B.B.; Hu, B.; Yen, H.W.; Cheng, G.J.; Wang, Z.K.; Luo, H.W.; Huang, M.X. High dislocation density–induced large ductility in deformed and partitioned steels. *Science* **2017**, *357*, 1029–1032. [CrossRef]
8. Neogi, A.; He, L.; Abdolrahim, N. Atomistic simulations of shock compression of single crystal and core-shell Cu@Ni nanoporous metals. *J. Appl. Phys.* **2019**, *126*, 015901. [CrossRef]
9. Fan, C.; Li, Q.; Ding, J.; Liang, Y.; Shang, Z.; Li, J.; Su, R.; Cho, J.; Chen, D.; Wang, Y.; et al. Helium irradiation induced ultra-high strength nanotwinned Cu with nanovoids. *Acta Mater.* **2019**, *177*, 107–120. [CrossRef]
10. Fu, H.; Ge, B.; Xin, Y.; Wu, R.; Fernandez, C.; Huang, J.; Peng, Q. Achieving High Strength and Ductility in Magnesium Alloys via Densely Hierarchical Double Contraction Nanotwins. *Nano Lett.* **2017**, *17*, 6117–6124. [CrossRef] [PubMed]
11. Wei, Y.; Li, Y.; Zhu, L.; Liu, Y.; Lei, X.; Wang, G.; Wu, Y.; Mi, Z.; Liu, J.; Wang, H.; et al. Evading the strength–ductility trade-off dilemma in steel through gradient hierarchical nanotwins. *Nat. Commun.* **2014**, *5*, 3580. [CrossRef] [PubMed]

12. Zheng, X.; Xie, W.; Zeng, L.; Wei, H.; Zhang, X.; Wang, H. Achieving high strength and ductility in a heterogeneous-grain-structured CrCoNi alloy processed by cryorolling and subsequent short-annealing. *Mater. Sci. Eng. A* **2021**, *821*, 141610. [CrossRef]
13. Zhang, D.; Qiu, D.; Gibson, M.A.; Zheng, Y.; Fraser, H.L.; StJohn, D.H.; Easton, M.A. Additive manufacturing of ultrafine-grained high-strength titanium alloys. *Nature* **2019**, *576*, 91–95. [CrossRef] [PubMed]
14. Wang, L.; Fan, X.; Lu, F.; Liang, Y.; Li, S. Improving the formability and mechanical properties of TiAl alloy by direct forging of uncondensed powder. *Mater. Sci. Eng. A* **2024**, *890*, 145890. [CrossRef]
15. Zhou, L.; Fang, H.; Yang, X.; Chen, R.; Yan, Y.; Zhang, Y.; Su, Y.; Guo, J. Adjusting the γ/α_2 and Ti_2AlC phase on microstructure evolution and improving mechanical properties at room and elevated temperatures with the addition of Ta. *Intermetallics* **2022**, *146*, 107579. [CrossRef]
16. Kurama, H.; Erkuş, Ş.; Gaşan, H. The effect of process control agent usage on the structural properties of MgB_2 synthesized by high energy ball mill. *Ceram. Int.* **2017**, *43*, S391–S396. [CrossRef]
17. Shu, S.; Qiu, F.; Xing, B.; Jin, S.; Wang, Y.; Jiang, Q. Study of effect of Mn addition on the mechanical properties of Ti_2AlC/TiAl composites through first principles study and experimental investigation. *Intermetallics* **2012**, *28*, 65–70. [CrossRef]
18. Radovic, M.; Barsoum, M.W. MAX phases: Bridging the gap between metals and ceramics MAX phases: Bridging the gap between metals and ceramics. *Am. Ceram. Soc. Bull.* **2013**, *92*, 20–27.
19. Chen, R.; Tan, Y.; Fang, H.; Luo, L.; Ding, H.; Su, Y.; Guo, J.; Fu, H. Macro/microstructure evolution and mechanical properties of Ti33.3Al alloys by adding WC particles. *Mater. Sci. Eng. A* **2018**, *725*, 171–180. [CrossRef]
20. Shu, S.; Qiu, F.; Jin, S.; Lu, J.; Jiang, Q. Compression properties and work-hardening behavior of Ti_2AlC/TiAl composites fabricated by combustion synthesis and hot press consolidation in the Ti–Al–Nb–C system. *Mater. Des.* **2011**, *32*, 5061–5065. [CrossRef]
21. Cheng, J.; Zhu, S.; Yu, Y.; Yang, J.; Liu, W. Microstructure, mechanical and tribological properties of TiAl-based composites reinforced with high volume fraction of nearly network Ti_2AlC particulates. *J. Mater. Sci. Technol.* **2018**, *34*, 670–678. [CrossRef]
22. Luo, Y.-F.; Lu, R.-Y.; Wang, Y.; Liu, B.; Yang, H.-T.; Liu, Y. Interfacial reaction in Al_2O_3 fiber reinforced TiAl matrix composite. *Trans. Nonferr. Met. Soc. China* **2023**, *33*, 2054–2063. [CrossRef]
23. Kan, W.; Chen, B.; Peng, H.; Liang, Y.; Lin, J. Fabrication of nano-TiC reinforced high Nb-TiAl nanocomposites by electron beam melting. *Mater. Lett.* **2020**, *259*, 126856. [CrossRef]
24. Yan, H.-J.; Meng, X.-Z.; Zhuang, Z.-T.; Zhang, Q.-H.; Sun, Q.-Q.; Wu, L.-K.; Cao, F.-H. Effect of Ni in SiO_2 coating on the oxidation resistance of TiAl alloy at 900 °C. *Appl. Surface Sci.* **2023**, *638*, 158054. [CrossRef]
25. Wang, Y.; Ma, T.; Chen, Z.; Zhang, X.; Wang, X.; Zhu, D.; Fang, H.; Chen, R. Superior high-temperature strength-ductility of TiB_2–Ti_2AlN/TiAl composite with core-shell microstructure. *Mater. Sci. Eng. A* **2024**, *889*, 145873. [CrossRef]
26. Li, X.; Zhang, W. Interfacial reaction in SiC_f/C/TiAl matrix composites. *J. Mater. Res. Technol.* **2021**, *12*, 1227–1234. [CrossRef]
27. Cai, Z.H.; Zhang, D.L. Sintering behaviour and microstructures of Ti(Al,O)/Al_2O_3, Ti_3Al(O)/Al_2O_3 and TiAl(O)/Al_2O_3 in situ composites. *Mater. Sci. Eng. A* **2006**, *419*, 310–317. [CrossRef]
28. Sousa, L.; Antunes, R.D.M.; Fernandes, J.C.S.; Alves, A.C.; Toptan, F. Influence of Al_2O_3 reinforcements and Ti-Al intermetallics on corrosion and tribocorrosion behavior of titanium. *Surface Coat. Technol.* **2023**, *470*, 129835. [CrossRef]
29. Huy, T.D.; Fujiwara, H.; Yoshida, R.; Binh, D.T.; Miyamoto, H. Microstructure and Mechanical Properties of $TiAl_3$/Al_2O_3 in situ Composite by Combustion Process. *Mater. Trans.* **2014**, *55*, 1091–1093. [CrossRef]
30. Lu, X.; Li, J.; Chen, X.; Qiu, J.; Wang, Y.; Liu, B.; Liu, Y.; Rashad, M.; Pan, F. Mechanical, tribological and electrochemical corrosion properties of in-situ synthesized Al_2O_3/TiAl composites. *Intermetallics* **2020**, *120*, 106758. [CrossRef]
31. Ma, M.; Liang, L.; Wang, L.; Wang, Y.; Cheng, Y.; Tang, B.; Xiang, W.; Tan, X. Phase transformations of titanium hydride in thermal desorption process with different heating rates. *Int. J. Hydrogen Energy* **2015**, *40*, 8926–8934. [CrossRef]
32. Schoenitz, M.; Zhu, X.; Dreizin, E.L. Carbide formation in Al–Ti mechanical alloys. *Scr. Mater.* **2005**, *53*, 1095–1099. [CrossRef]
33. Liu, P.; Hou, B.; Wang, A.; Xie, J.; Wang, Z. Balancing the strength and ductility of Ti_2AlC/TiAl composite with a bioinspired micro-nano laminated architecture. *Mater. Des.* **2022**, *220*, 110851. [CrossRef]
34. Cui, S.; Cui, C.; Lv, J.; Chen, S.; Xie, J.; Liu, S. Fabrication, microstructure and mechanical properties of Al_2O_3 whiskers reinforced Ti-46Al-4Nb alloy. *Mater. Lett.* **2020**, *259*, 126902. [CrossRef]
35. Cui, S.; Cui, C.; Yang, S.; Liu, S. Microstructure and mechanical properties of hybrid in-situ Ti_2AlC_w/Mo_2B_{5p} reinforced TiAl alloy. *Mater. Sci. Eng. A* **2022**, *829*, 142182. [CrossRef]
36. Barsoum, M.W.; El-Raghy, T.; Ali, M. Processing and characterization of Ti_2AlC, Ti_2AlN, and $Ti_2AlC0.5N0.5$. *Metall. Mater. Trans. A* **2000**, *31*, 1857–1865. [CrossRef]
37. Youn, S.-J.; Kim, Y.-K.; Kim, S.-W.; Lee, K.-A. Elevated temperature compressive deformation behaviors of γ-TiAl-based Ti–48Al–2Cr–2Nb alloy additively manufactured by electron beam melting. *Intermetallics* **2020**, *124*, 106859. [CrossRef]
38. Gao, Y.-L.; Kou, S.-Q.; Dai, J.-N.; Wang, Z.-F.; Shu, S.-L.; Zhang, S.; Qiu, F.; Jiang, Q.-C. Microstructural configuration and compressive deformation behavior of a TiAl composite reinforced by Mn and in situ Ti_2AlC particles. *Mater. Sci. Eng. A* **2021**, *823*, 141772. [CrossRef]
39. Song, X.; Cui, H.; Han, Y.; Ding, L.; Song, Q. $Ti_2Al(C, N)$ Solid Solution Reinforcing TiAl-Based Composites: Evolution of a Core–Shell Structure, Interfaces, and Mechanical Properties. *ACS Appl. Mater. Interfaces* **2018**, *10*, 16783–16792. [CrossRef] [PubMed]

40. Wei, L.; Liu, J.; Wu, X.; Liu, X.; Lv, X.; Liu, Y. In situ fabrication of Ti-Al/Ti_2AlC composite by hot-press sintering. *J. Alloys Compd.* **2020**, *813*, 152200. [CrossRef]
41. Shu, S.; Qiu, F.; Lü, S.; Jin, S.; Jiang, Q. Phase transitions and compression properties of Ti_2AlC/TiAl composites fabricated by combustion synthesis reaction. *Mater. Sci. Eng. A* **2012**, *539*, 344–348. [CrossRef]
42. Zhu, D.; Liu, L.; Dong, D.; Wang, X.; Liu, Y.; Chen, Z.; Wei, Z. Microstructure and compression behavior of in-situ synthesized Ti_2AlC reinforced Ti-48Al-2Cr alloy with carbon nanotubes addition. *J. Alloys Compd.* **2021**, *862*, 158646. [CrossRef]
43. Rester, M.; Fischer, F.D.; Kirchlechner, C.; Schmoelzer, T.; Clemens, H.; Dehm, G. Deformation mechanisms in micron-sized PST TiAl compression samples: Experiment and model. *Acta Mater.* **2011**, *59*, 3410–3421. [CrossRef]
44. Vinogradov, A.; Heczko, M.; Mazánová, V.; Linderov, M.; Kruml, T. Kinetics of cyclically-induced mechanical twinning in γ-TiAl unveiled by a combination of acoustic emission, neutron diffraction and electron microscopy. *Acta Mater.* **2021**, *212*, 116921. [CrossRef]
45. Afrin, N.; Chen, D.L.; Cao, X.; Jahazi, M. Strain hardening behavior of a friction stir welded magnesium alloy. *Scr. Mater.* **2007**, *57*, 1004–1007. [CrossRef]